



# Fatigue strength and microstructure evaluation of Al 7050 alloy wires recycled by spray forming, extrusion and rotary swaging

João G. J. de SALVO<sup>1,2</sup>, Conrado R. M. AFONSO<sup>3</sup>

1. Programa de Pós-graduação em Ciência e Engenharia de Materiais (PPG-CEM),  
Universidade Federal de São Carlos (UFSCar), Rod. Washington Luiz, Km 235, 13565-905 São Carlos - SP, Brazil;

2. Divisão de Materiais, Instituto de Aeronáutica e Espaço, CTA,

Praça Marechal Eduardo Gomes, 50, 12228-904 São José dos Campos - SP, Brazil;

3. Departamento de Engenharia de Materiais (DEMa), Universidade Federal de São Carlos (USFCar),

Rod. Washington Luiz, Km 235, 13565-905 São Carlos - SP, Brazil

Received 17 February 2020; accepted 22 October 2020

**Abstract:** Recycled high-strength aluminum alloys have limited use as structural materials due to poor mechanical properties. Spray forming remelting followed by hot extrusion is a promising route for reprocessing 7xxx alloys. The 7050 alloy machining chips were spray formed, hot extruded, rotary swaged and heat-treated in order to improve mechanical properties. Microstructures, tensile properties and fatigue strength results for a 2.7 mm-diameter recycled wire are presented. Secondary phases and precipitates were investigated by XRD, SEM, EBSD, TEM and DSC. As-swaged and heat-treated (solution and aging) conditions were evaluated. Mechanical properties of both conditions outperformed AA7050 aerospace specification. Substantial grain refinement resulted from the extensive plastic deformation imposed by rotary swaging. Refined micrometric and sub-micrometric Al grains, as well as coarse and fine intermetallic precipitates were observed. Subsequent solution treatment resulted in a homogeneous, recrystallized and equiaxed microstructure with grain size of 9  $\mu\text{m}$ . Nanoscale GP(I) zones and  $\eta'$  phase precipitates formed after aging at 120 °C, imparting higher tensile (586 MPa) and fatigue (198 MPa) strengths.

**Key words:** Al–Zn–Mg–Cu alloy; spray forming; thermomechanical processing; microstructure; fatigue

## 1 Introduction

Aluminum alloys of the Al–Zn–Mg–(Cu) system (7000 series) respond strongly to age hardening and have high specific strength, ductility, toughness, fatigue resistance and stress corrosion cracking resistance. These properties enable these alloys to be widely used in aircraft structural parts [1]. The process of machining thick plates of 7050 alloy is commonly used for producing fuselage frames, bulkheads and other structural parts, yielding huge amounts of machining chip waste due to the low efficiency of the process [2].

The usual destination of this noble alloy is the secondary aluminum industry, where it is remelted to complete the chemical composition of low performance cast alloys. However, such a high valuable waste has a greater application potential if properly recycled. Therefore, there is a technological opportunity to be evaluated, with associated lower energy consumption and reduced carbon footprint [3]. Chemical composition, processing parameters, and the microstructure affecting mechanical behavior are some of the most important factors considered, not only in designing high strength aluminum alloy [4], but also in the recycling context. The latter, may represent a more

challenging situation owing to reprocessing limitations and a possible introduction of contaminants. Advanced processes may be required in order to obtain the mechanical properties of the original alloy. High-strength 7000 aluminum alloys are usually high-alloyed materials with considerable tendency to segregation and hot tearing [1,5]. Hence, conventional ingot metallurgy, usually associated with coarse grains and macrosegregation, seems unsuitable for this purpose, resulting in a low performance material.

Spray forming has been shown to be an effective process to reduce segregation and control intermetallic morphology, thus improving the strength and ductility of gas atomized aluminum alloys [5]. Subsequent hot extrusion yields even higher ductility due to the porosity closure effect [6]. SHARMA [7] has pointed out the advantage of spray forming to provide better mechanical properties without adversely affecting the ductility of 7000 series alloys. Previous studies on recycling of 7050 alloy machining chips [2,8–11] have shown that spray forming remelting followed by hot extrusion may be an effective technological route for converting aluminum scrap into semi-finished products, whose properties are compatible with those provided by the original alloy. The refined intermetallics, increased solid solubility, low segregation and fine-grained microstructure typical for spray deposited metals [12] allow for higher mechanical properties and homogenization heat treatment of the alloy to be shortened or avoided [13]. The refinement of deleterious Fe bearing constituent particles is of special interest to the recycling of Al alloys, which are subjected to an increase in Fe content arising primarily from scrap handling equipment [3], and also from machining processes. Regarding hot extrusion, the imposed compressive forces admit high levels of plastic strain with low cracking risk, which makes it an efficient process to change the as-deposited structure and reduce residual porosity of spray-formed alloys [2,6,11]. Further rotary swaging processing of extruded Al alloys can lead to substantial grain refinement through the imposition of severe plastic deformations [14], with improved fatigue performance [15,16].

GUERRA et al [11] have studied the reprocessing of 7050 alloy by spray forming, hot

extrusion and rotary swaging. However, the secondary phases presented after rotary swaging were not identified nor characterized. Moreover, the optimization of mechanical properties by aging heat treatment was not investigated. In order to qualify the material for practical structural application, it is essential to provide fatigue performance data of recycled high strength aluminum alloys. In this study, AA7050 machining chips were re-melted and spray formed, followed by hot extrusion, rotary swaging and heat treatments to optimize monotonic and cyclic mechanical properties. Considering the possibility of reintroducing this recycled material in manufacturing overhead transmission cables, this processing route aimed to produce 2.7 mm-diameter wires as a semi-finished product. An effort was undertaken to characterize the secondary phases and precipitates and to provide fatigue strength data for the recycled 7050 alloy. The mechanical behavior was evaluated from room temperature tensile and fatigue testing, and the results were correlated to the microstructural features resulting from the thermomechanical processing history.

## 2 Experimental

### 2.1 Material

AA7050 machining chips provided by the aircraft industry were melted under nitrogen atmosphere in an induction furnace coupled to a semi-industrial spray forming equipment. A more detailed description and parameters of the spray forming and thermomechanical processing are given in Ref. [11]. The as-deposited billet was machined to 107 mm in diameter and 200 mm in length and subsequently subjected to a double-step homogenization heat treatment, which consisted of 4 h at 420 °C and 8 h at 470 °C. It was followed by water quenching in order to avoid uncontrolled precipitation. Then, the billet was hot extruded at 420 °C and at an extrusion ratio of 179:1 into cylindrical rods of 8 mm in diameter. The extruded rods were then subjected to three reduction steps in a rotary swaging machine, producing a final 2.7 mm-diameter wire. The total accumulated true strain ( $\varphi$ ) calculated from the cross sectional area reduction for the cold rotary swaging process was 2.17 ( $\varphi = \ln(A_0/A)$ , where  $A_0$  is the initial cross section area and  $A$  is the final cross section area).

The material condition after the thermomechanical processing was called “as-swaged condition”. Part of this material was further solution-treated at 470 °C for 0.5 h, water quenched, and artificially aged at 120 °C for 6 h; namely “aged condition”. After the aging treatment, the material was allowed to cool in calm air. The chemical composition of the produced AA7050 wire was 6.07% Zn, 1.93% Mg, 2.15% Cu, 0.08% Zr, 0.08% Fe, 0.05% Si and balanced Al (wt.%), as determined by inductively coupled plasma optical emission spectrometry (ICP-OES).

## 2.2 Microstructure characterization

Both distinct microstructures obtained, under as-swaged and aged conditions, were investigated by X-ray diffraction (XRD) (Philips PANalytical X’Pert Pro 3060 diffractometer), and scanning electron microscopy (SEM) (LEO 435 VPi coupled to Oxford energy dispersive X-ray spectroscopy–EDS); SEM–EBSD–EDS simultaneous analysis was realized in a ZEISS dual beam model AURIGA Compact (field emission gun–FEG electron beam and Ga source focused ion beam–FIB), which was also used for FIB “in-situ” polishing of a wire sample surface previous to EBSD map acquisition at 15 kV. Transmission electron microscopy (TEM) was carried out using a Tecnai G2F20 TEM/STEM with a field emission gun operating at 200 kV, coupled to an EDAX EDS detector. Metallographic specimens for SEM analysis were ground, polished and etched using Keller’s etchant for approximately 15 s to reveal the microstructure. The average grain size was estimated by the intercept procedure according to the ASTM E112 standard [17]. Porosity and second phase area fraction were determined by image analysis software. Specimens for TEM were 2.7 mm in diameter and had their thickness reduced to 0.1 mm. They were finally thinned by double-jet electropolishing with a 30% nitric acid solution in methanol at –20 °C and 15 V. Differential scanning calorimetry (DSC) thermal analyses were carried out using a NETZSCH 404 Maia, under argon flow atmosphere, and with a constant heating rate of 20 K/min and pure Al used for the baseline.

## 2.3 Mechanical testing

Tensile and fatigue tests were performed at

room temperature using specimens that consisted of 160 mm-length sections of the 2.7 mm-diameter recycled wire, which were longitudinally loaded. The as-swaged surface finishing of the specimens was preserved, i.e., specimens were tested without any previous surface preparation or modification. Tensile tests were performed in a MTS machine at a constant crosshead speed of 1.2 mm/min; at least three samples for each condition were tensile tested. Axial fatigue tests were performed in a MTS Landmark tabletop servohydraulic testing machine at constant amplitude load condition by means of a sinusoidal stress wave at frequency of 40 Hz. This investigation considers the possibility of applying the recycled wires as reinforcement in overhead transmission cables. Therefore, a minimum stress level of 100 MPa was fixed, which represents the constant service load of conventional cable wires under normal conditions of use, according to the Brazilian standards for reinforced transmission cables ABNT NBR 5422 and 7270. The maximum stress level ( $\sigma_{\max}$ ) varied from 150 to 210 MPa; therefore, the stress ratio  $R$  ranged from 0.48 to 0.67. The staircase method established by the ISO 12107: 2012 standard [18] was applied to conducting the fatigue tests. It is considered a remarkably accurate and efficient method to quantify the mean fatigue strength, even for samples as small as 5–10 specimens [19]. Its statistical analysis is based on the Dixon–Mood equations [20] to estimate the mean and standard deviation values of fatigue strength, which is assumed as a statistical variable that follows a normal distribution. A detailed description of the method is given in Ref. [21]. In this study, ten specimens were tested for each condition to estimate the average fatigue strength corresponding to a high cycle fatigue life of  $10^6$  cycles. Initially, in order to roughly estimate the fatigue strength, three specimens were spent for preliminary experiments for each condition. The goal was to concentrate the tests around the average strength value, consequentially enhancing the accuracy of the method. Ultimately, seven specimens from each condition were effectively considered for the statistical analysis. A 10 MPa increment was set. According to the performance of each new test specimen, i.e., if it survived or failed, the maximum stress level in the test with the subsequent test

specimen was increased or decreased by 10 MPa, respectively. Testing was stopped after  $10^6$  cycles were applied to the specimen, or when the specimen failed by complete separation. Composite material tabs were used to avoid stress concentration and eliminate fracture occurrence at the gripped region of the specimens.

### 3 Results and discussion

#### 3.1 Microstructure

Figure 1 shows the microstructure of the reprocessed 7050 aluminum alloy as-swaged wire. It reveals a highly deformed and non-recrystallized microstructure with elongated and refined grains less than  $1\ \mu\text{m}$  wide and a few microns long. The severe plastic deformation (true strain of 2.17) combined with the lack of recrystallization in the cold rotary swaging process yielded homogeneous microstructural refinement. This may be noticeable when compared to previous investigations on recycled 7050 hot-extruded bars [2,8,10,11], in which partial recrystallization and coarse-grained regions are reported. Bright second phase particles of  $0.5\text{--}3\ \mu\text{m}$  could also be seen to evenly distribute throughout the matrix. BSE signal image acquisition enabled secondary phase differentiation from the matrix, whereby an average value of 2.5% in the area was determined by quantitative metallographic image analysis. In general, only a few dispersed coarse constituent particles ( $>5\ \mu\text{m}$ ) were observed, for which the EDS chemical analysis (Table 1) indicated the  $\text{Al}_7\text{Cu}_2\text{Fe}$  constituent particle. Image analysis also revealed 0.4% porosity area. Chemical etching removed part of the secondary phase particles, which led to overestimated values of porosity. Nevertheless,

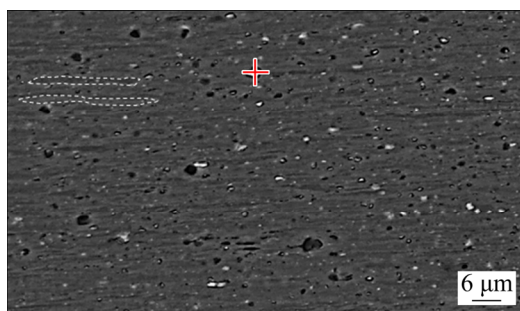


**Fig. 1** SEM image in BSE mode showing microstructure of longitudinal cross-section of 2.7 mm-diameter as-swaged wire

**Table 1** EDS analysis results of coarse precipitates of as-swaged wire (at.%)

Phase	Al	Zn	Mg	Cu	Fe	Si
Matrix	94.1	2.5	2.2	1.1	–	–
Coarse precipitates	64.7	0.6	–	20.7	13.4	0.5

when compared to 3.6% porosity level in the as-deposited material [11], a substantial porosity closure ( $\sim 90\%$ ) was obtained after thermo-mechanical processing of the deposit by hot extrusion and rotary swaging.

The XRD diffraction pattern of the as-swaged wire is presented in Fig. 2 showing the intermetallic phases of  $\text{Al}_7\text{Cu}_2\text{Fe}$ ,  $\text{Al}_2\text{CuMg}$ , and  $\text{MgZn}_2$  ( $\eta$  phase), besides the Al-fcc matrix. The  $\text{Al}_7\text{Cu}_2\text{Fe}$  detection corroborates the EDS results for the coarse constituent particles. This undesirable intermetallic is associated to lower ductility and toughness, and is usually pointed out as an initiation site and/or preferential path for fatigue crack in high-strength aluminum alloys [22]. High-temperature homogenization heat-treatment commonly yields fast and complete dissolution of the  $\eta$  ( $\text{MgZn}_2$ ) phase and partial sluggish dissolution of the  $S$  ( $\text{Al}_2\text{CuMg}$ ) phase [23]. Hence, the presence of the  $\eta$  phase in the as-swaged condition suggests it precipitated dynamically or during the slow cooling from hot extrusion as the billet was double-step homogenized at 420 and 470 °C before the extrusion process.

Figures 3 and 4 illustrate the SEM–EBSD–EDS simultaneous analysis results of a longitudinal

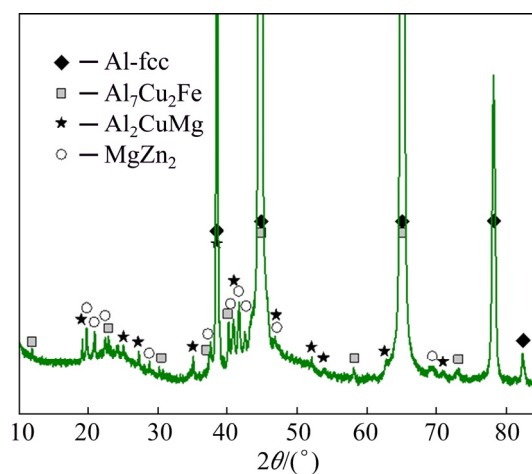


**Fig. 2** XRD pattern of as-swaged wire showing peaks of intermetallic phases of  $\text{Al}_7\text{Cu}_2\text{Fe}$ ,  $\text{Al}_2\text{CuMg}$  and  $\text{MgZn}_2$  ( $\eta$  phase), besides Al-fcc matrix

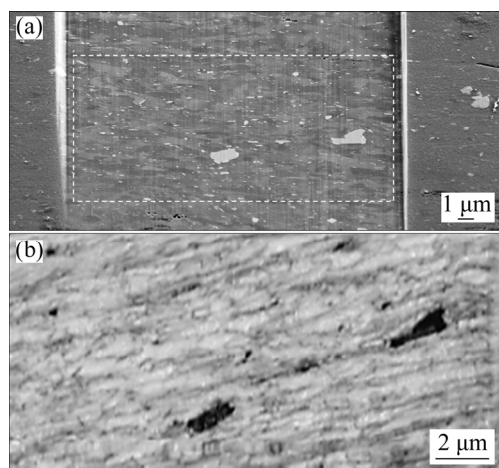


**Fig. 3** SEM images of longitudinal section of as-swaged wire, showing backscattered electron diffraction (EBSD) results: (a) SEM image of FIB polished surface; (b) Band contrast image (BC)

section of as-swaged 2.7 mm-diameter wire of 7050 alloy, starting with the SEM image of the FIB polished surface (Fig. 3(a)) revealing very refined micrometric and sub-micrometric Al-fcc grains, as well as coarse and fine intermetallic precipitates. Figure 3(b) presents an EBSD analysis with a band contrast image (BC) showing identified brighter Al-fcc grains and darker particles not indexed by the detector probably due to fragmentation of precipitates after rotary swaging deformation. Figure 4(a) presents an IPF orientation map on the  $X$ -axis showing preferential orientation around the [111] direction. Figure 4(b) presents an EBSD phase map analysis showing Al-fcc phase (red) and precipitates of  $MgZn_2$  intermetallic (green), respectively. The same region of EBSD (white dotted line in Fig. 3(a)) is shown in Fig. 4(c) in the SEM image and respective X-ray elemental maps acquired by the SEM-EDS simultaneously with the EBSD analysis for Al-fcc matrix and precipitates of  $Al_7Cu_2Fe$  and  $MgZn_2$  intermetallic phases.

Through the conventional metallographic preparation of samples for EBSD, by 1  $\mu m$  and then 0.3  $\mu m$  diamond paste polishing, in addition to the automatic vibration polishing (Vibromet Büehler) with colloidal silica of 0.05  $\mu m$  (50 nm), the surface of wire sample seemed polished and suitable for EBSD analysis. However, at the moment of acquiring the Kikuchi patterns, the quality was far from the ideal (less than 50% indexing), making it

difficult to identify the phases, mainly the Al-fcc matrix resulting in poor EBSD maps. The reasons for that would be highly deformed grains and surface Al oxide layer after sample preparation. Just after polishing the sample surface by focused ion beam (FIB) in-situ inside the dual beam microscope, the quality of Kikuchi lines was improved and the phases during EBSD patterns were identified. Thus, using a step of 0.03  $\mu m$  (30 nm), it was possible to acquire the EBSD map, even after rotary swaging deformation reached the limit of the EBSD technique. Using an advanced tool through FIB inside the microscope (dual beam model) in a vacuum, for the surface polishing of the region to be analyzed, was very effective in order to optimize the acquisition of Kikuchi patterns and a map with much better quality (~90% of Al-fcc phase indexing). Only the micrometric  $Al_7Cu_2Fe$  fragmented precipitates were not well indexed during analysis.

SPD techniques can produce a significant modification to the precipitation microstructure of metallic materials [24,25]. It has been shown for SPDed Al-Zn-Mg-Cu alloys that Mg and Cu strongly segregate at the grain and subgrain boundary [26]. The solute redistribution and the segregation at grain boundaries affect precipitation behavior during subsequent aging. In the present investigation, there was no evidence of significant solute segregation from rotary swaging. However, the presence of coarse equilibrium  $\eta$  precipitates, as identified by XRD (Fig. 2), EBSD (Fig. 4(b)) and X-ray elemental maps (Figs. 4(d-h)), indicated heterogeneous nucleation. The high density of dislocations and grain and subgrain boundaries generated after swaging acted as favorable nucleation sites and fast diffusion paths for solute atoms, favoring heterogeneous nucleation of equilibrium precipitates.

A solution treatment was required in order to attain the high strength potential of the 7050 alloy by promoting the dissolution of soluble secondary phases, thus generating a supersaturated solid solution for further fine precipitation upon artificial aging. Figure 5(a) presents BSE image of a wire sample solution-treated for 0.5 h at 470 °C followed by water quenching. Fully recrystallized and equiaxed grains could be seen, indicating that the stored strain energy from cold working was

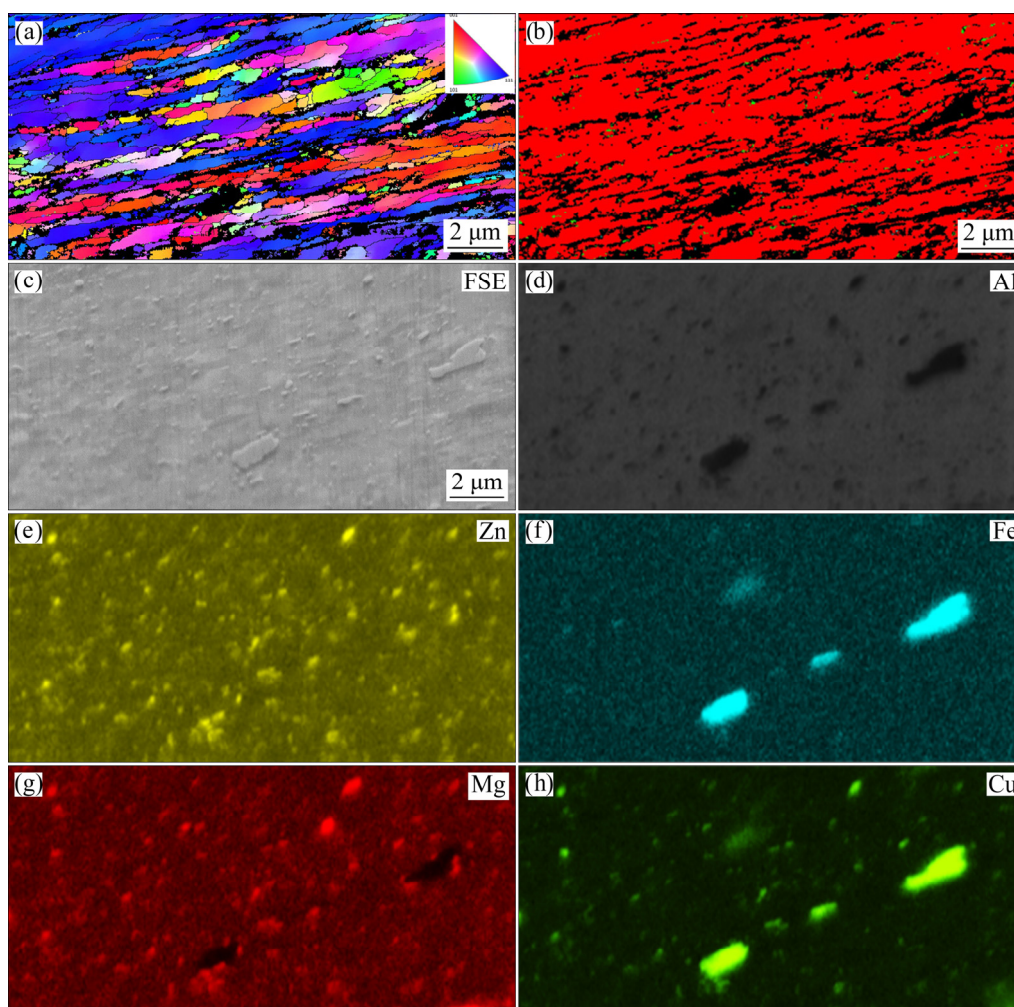


**Fig. 4** IPF orientation map on  $X$ -axis showing preferential orientation around  $[111]$  direction (a), EBSD phase map analysis result showing Al-fcc phase (red) and precipitates of  $MgZn_2$  intermetallic (green), respectively (b), SEM forward scattered electrons (FSE) image (c), and respective X-ray elemental maps acquired by SEM-EDS simultaneously with EBSD analysis for Al-fcc matrix and precipitates of  $Al_7Cu_2Fe$  and  $MgZn_2$  intermetallic phases ((d) Al, (e) Zn, (f) Fe, (g) Mg and (h) Cu)

sufficient to promote the formation of new grains, which grew to an average size of  $9 \mu m$ . There was not a noticeable grain size variation from the surface to the core of the wire, indicating that rotary swaging process was able to promote homogeneous deformation along the cross section.

The heat treatment conditions were not sufficient to dissolve  $Al_7Cu_2Fe$  constituent particles, as revealed in Fig. 5(b). Nevertheless, the area fraction of secondary phases was substantially reduced from 2.5% in the as-swaged condition to 1.0% after solution treatment. Thereby, most of the second phase particles were dissolved without leading to grain coarsening or incipient melting. SPD increases both defect density and grain

boundary volume, consequently increasing the diffusion rate of solute atoms. This may have favored rapid dissolution of secondary phases during the solution treatment, which was effective despite being relatively short (0.5 h). Solution heat treating at  $470 \text{ }^\circ C$  was pointed out by HAN et al [27] as the most efficient single-stage treatment regarding tensile strength and fracture toughness of 7050 Al alloy, since these properties are given by a balance between precipitation strengthening and fine grain strengthening.

XRD patterns of the solution-treated and aged samples are shown in Fig. 6. The subsequent artificial aging at  $120 \text{ }^\circ C$  for 6 h resulted in an

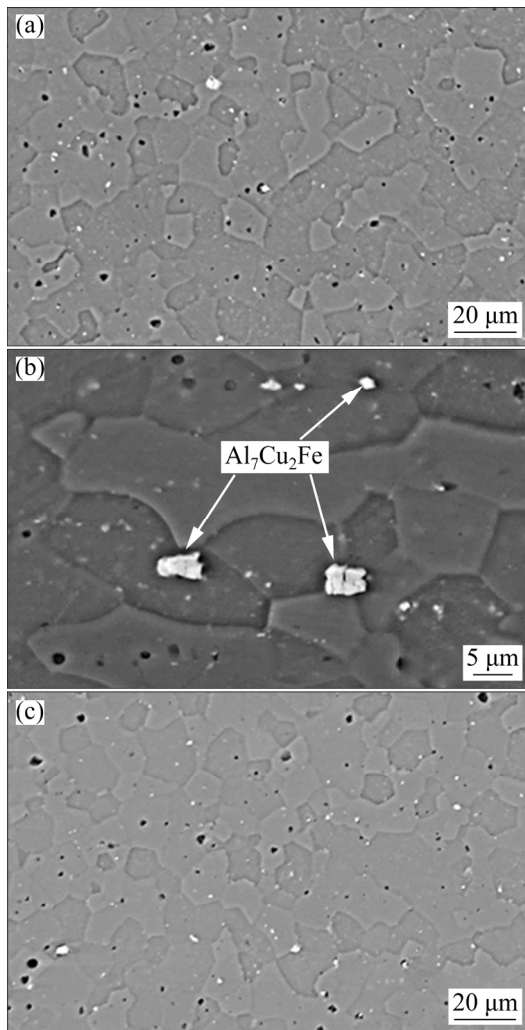


**Fig. 5** SEM–BSE images showing microstructures of cross-section of solution-treated wire (a, b) and aged wire (c)

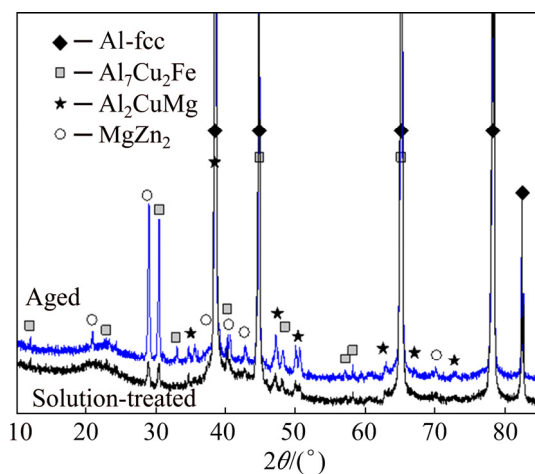


**Fig. 6** XRD patterns of solution-treated and aged wire showing increased volume fraction of  $MgZn_2$ ,  $Al_7Cu_2Fe$  and  $Al_2CuMg$  intermetallic precipitates

increased volume fraction of secondary phases, as indicated by the higher intensity peaks on the diffraction pattern of the aged condition. The increased volume fraction of  $MgZn_2$ ,  $Al_7Cu_2Fe$  and  $Al_2CuMg$  is attributed to the precipitation process. SEM observations showed no significant difference between the microstructure of the aged condition (Fig. 5(c)), as compared to the solution-treated condition (Fig. 5(a)). The study of the fine precipitates in the aged condition was carried out by DSC and TEM investigations.

Figure 7 shows the SEM analysis results of a longitudinal section of 2.7 mm-diameter wire of 7050 alloy after aging, showing backscattered electron diffraction (EBSD) results. Figure 7(a) presents a forward scattered electron (FSE) image, and Fig. 7(b) illustrates an IPF orientation map on the  $X$ -axis showing preferential orientation around the  $[111]$  direction. It is worth mentioning that the inner part of the sample was polished by FIB in-situ inside a dual beam microscope, resulting in much better quality of Kikuchi lines and identification of phases during EBSD pattern acquisition. The improvement of EBSD pattern quality can be clearly observed in the Fig. 7(b) (IPF orientation image). The X-ray elemental maps were acquired by SEM–EDS simultaneously with the EBSD analysis showing fine scale precipitates of the  $Al_7Cu_2Fe$  intermetallic phase.

### 3.2 DSC thermal analysis

Differential scanning calorimetry (DSC) thermal analysis was used to investigate the precipitation process of 7xxx alloys [28–31]. Exothermic and endothermic events on a DSC thermogram are related to precipitate formation and dissolution, respectively. The heat of reaction is measured by the area under the curve and is proportional to the volume fraction of precipitate formation/dissolution. The precipitation sequence after solution treatment of the Al–Zn–Mg–(Cu) system is often reported as follows [28,32]:

Supersaturated solid solution  $\rightarrow$  GP (Guinier Preston) zones  $\rightarrow$   $\eta'$  metastable phase  $\rightarrow$   $\eta$  equilibrium ( $MgZn_2$ )

Figure 8 shows the DSC traces for the 7050 recycled alloy in the as-swaged condition and after solution and aging heat treatments for comparison. The DSC analysis was focused on investigating fine precipitates at the reprocessed 7050 wires, thus the

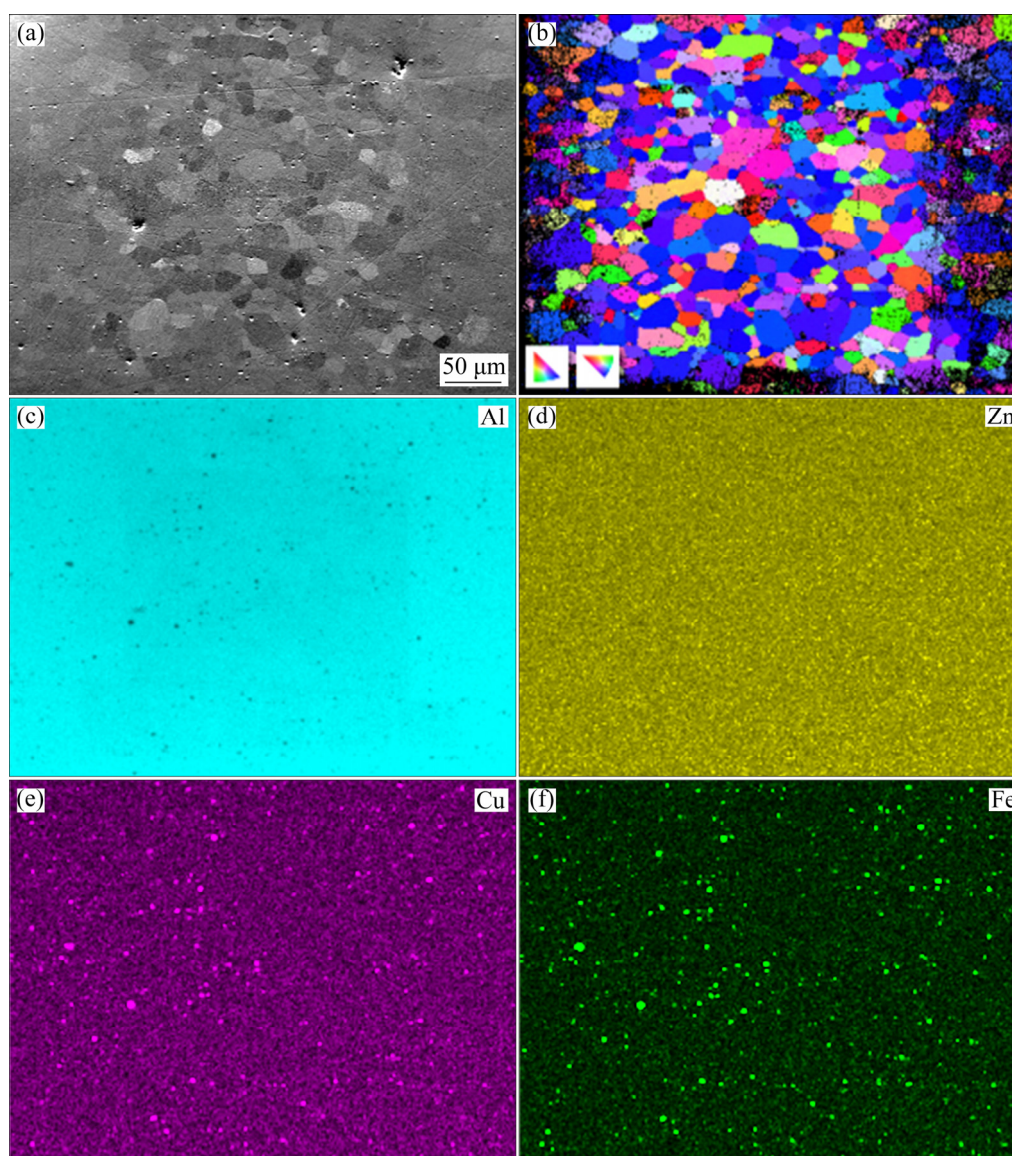


**Fig. 7** SEM analysis results of longitudinal section of 2.7 mm-diameter wire of 7050 alloy after aging, showing forward scattered electron (FSE) image (a), IPF orientation map on  $X$ -axis (preferential orientation around [111] direction) (b) and X-ray elemental maps acquired by SEM–EDS simultaneously with EBSD analysis showing fine scale precipitates of  $\text{Al}_7\text{Cu}_2\text{Fe}$  intermetallic phase ((c) Al, (d) Zn, (e) Cu and (f) Fe)

temperature range of interest was 50–300 °C. Initially, a broad endothermic peak ranging from ~60 to ~180 °C can be seen for the as-swaged condition. This peak is a superposition of Peaks 1 and 2, caused by the dissolution of zones GP(I) and GP(II), respectively [28,29]. This suggests there was a high solute concentration at the matrix of the wire immediately after the rotary swaging steps. Further natural aging resulted in the formation of a high volume fraction of GP zones in the as-swaged wire. During DSC heating, these zones were dissolved as indicated by the endothermic reaction. Both types of GP zones appeared in the as-swaged

condition. However, a higher volume fraction of GP(II) zones was revealed, which seems consistent with other DSC investigations on naturally aged 7xxx [28–31]. The wide temperature range of Peaks 1 and 2 indicates zones with different stabilities, i.e., there was a large zone size distribution. Carrying on heating, the small exothermic reaction Peak 3 is caused by the formation of  $\eta'$  phase from the GP zones. Moreover, the exothermic Peak 4 at 225 °C indicates the formation of  $\eta'$  and  $\eta$  phases by heterogeneous nucleation [30].

When compared to the as-swaged condition, the major differences observed for aged condition

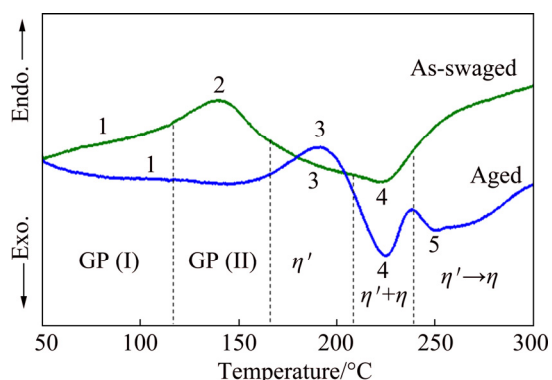


**Fig. 8** DSC curves of 7050 recycled alloy wire under as-swaged and aged conditions, showing peaks related to phase transformations and precipitation of main intermetallic phases

are the disappearance of Peak 2 and the appearance of a prominent endothermic Peak 3 ( $\eta'$  phase dissolution). These results indicate that the aging treatment at 120 °C yields the precipitation of GP(I) zones and a high volume fraction of  $\eta'$  phase; the latter precipitate is reported as the main strengthening precipitate in 7xxx alloys [4]. The absence of a GP(II) dissolution peak suggests that GP(I) has a more significant role in artificial aging at 120 °C. Finally, the exothermic Peak 4 is caused by the formation of  $\eta'$  and  $\eta$  phases. Furthermore, exothermic Peak 5 may be due to the transformation of  $\eta'$  to  $\eta$  equilibrium precipitate at higher temperatures [29]. The endothermic tendency above 250 °C for the curves of both conditions is caused by the dissolution of the remaining phases of the Al–Zn–Mg–Cu system.

### 3.3 TEM analysis on aged 7050 wire

The identification of the nanometric precipitates indicated in the DSC curve for the aged condition was carried out using the selected area diffraction (SAD) technique. Figure 9 presents the SAD patterns of three specific zone axes. Strong and defined spots are caused by the Al-fcc matrix. The diffuse scattering patterns receive special attention as they are able to identify fine precipitates. GP(I) zones are revealed in  $\langle 001 \rangle_{\text{Al}}$  direction as weak spots at  $\{1, (2n+1)/4, 0\}$  positions [33,34]. Spots from regions  $1/3$  and  $2/3\{220\}$  of zone axes  $\langle 001 \rangle_{\text{Al}}$  and  $\langle 112 \rangle_{\text{Al}}$  indicate the  $\eta'$  phase precipitation [11]. The metastable  $\eta'$  and equilibrium  $\eta$  phases are observable as streaks in the  $\langle 112 \rangle_{\text{Al}}$  and small spots in the direction close

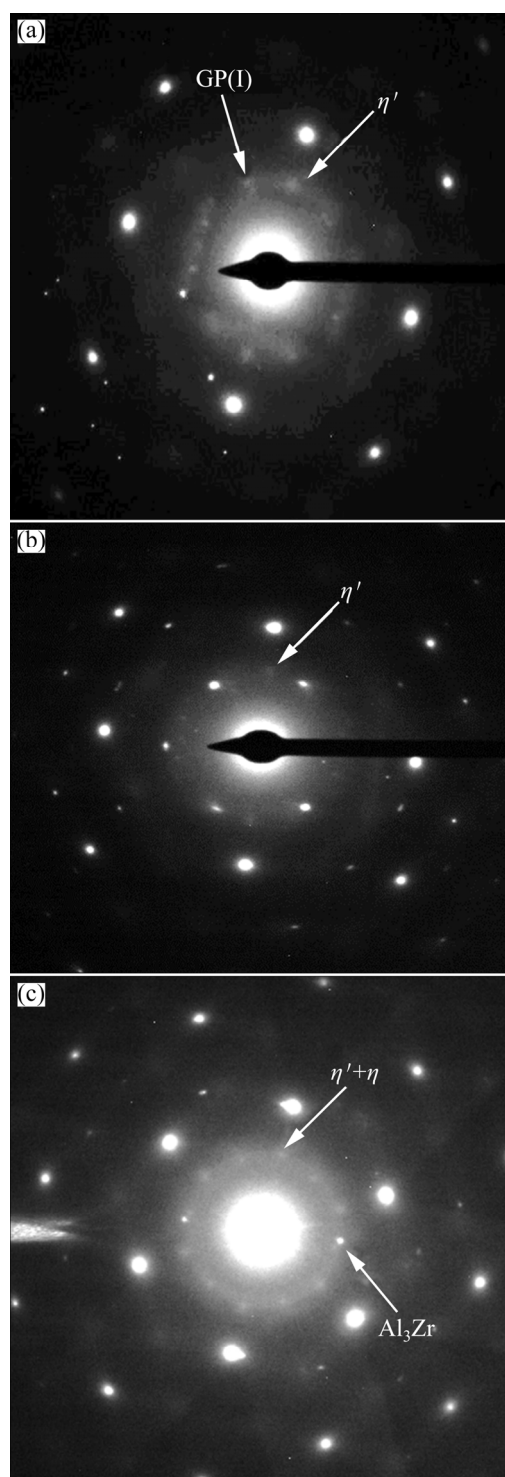


**Fig. 9** SAD patterns of aged condition zone axes: (a)  $\langle 001 \rangle_{\text{Al}}$ ; (b)  $\langle 112 \rangle_{\text{Al}}$ ; (c)  $\langle 111 \rangle_{\text{Al}}$

to the  $2/3\{220\}$  in  $\langle 111 \rangle_{\text{Al}}$  zone axis [8]. Diffraction spots from the  $\eta$  phase can be seen to be poorly defined. Thus, the SAD analysis indicated the GP(I) zones and the metastable hardening  $\eta'$  phase as the predominant precipitates under the aging condition at 120 °C, which corroborates the DSC results. Other authors [8,10] have also reported similar

conclusions for TEM investigation on 7050 alloy aged at 120 °C.

Furthermore, GP(II) diffraction spots usually pointed near position  $1/2\{311\}$  at  $\langle 112 \rangle_{Al}$  axis were not observed [32], indicating that GP(II) zones are not present in the 120 °C-aged condition. The small sharp spots in  $\langle 111 \rangle_{Al}$  are probably caused by the cubic  $Al_3Zr$  dispersoids [7]. It is well known from reciprocal space properties of electron diffraction (back focal plane) that the more diffuse (broader) the SAD spot, the smaller the precipitate in nanoscale in real space (TEM image), and as the diffraction spot becomes sharper, the precipitate becomes better defined in the TEM image (greater in size).

Figure 10 shows TEM images of precipitates in the matrix (Fig. 10(a)) and at grain boundary (Fig. 10(b)). Nanometric precipitates ( $\sim 5$  nm) may be observed finely dispersed throughout the matrix, which are probably the strengthening precipitates of GP(I) and  $\eta'$ , as indicated in the DSC and SAD analyses. Due to their nanoscale sizes, these fine precipitates are difficult to differentiate in TEM

analysis. A rod-shape elongated precipitate of a size around  $80 \text{ nm} \times 400 \text{ nm}$  and several spherical precipitates ranging from 10 to 40 nm are also shown; the former was analyzed by X-ray elemental mapping through EDS and will be discussed next; the further ones are the randomly distributed spherical and coherent  $Al_3Zr$  dispersoids identified in the SAD analysis, and also revealed in the X-ray mapping (Figs. 10(d–g)).

Despite the fact that some slightly larger precipitates (compared to matrix precipitates) may be seen at the grain boundaries, the precipitate free zone (PFZ) was not clearly observed. The presence of a high density of fine precipitates uniformly dispersed throughout the matrix suggests that these structures nucleated homogeneously. Homogeneous nucleation of GP zones and the absence of PFZ were favored by the whole processing history of the alloy, followed by the low aging temperature (120 °C). Additionally, the previous high-temperature (470 °C) solution heat treatment immediately followed by water quenching is known to promote the supersaturation of alloying elements

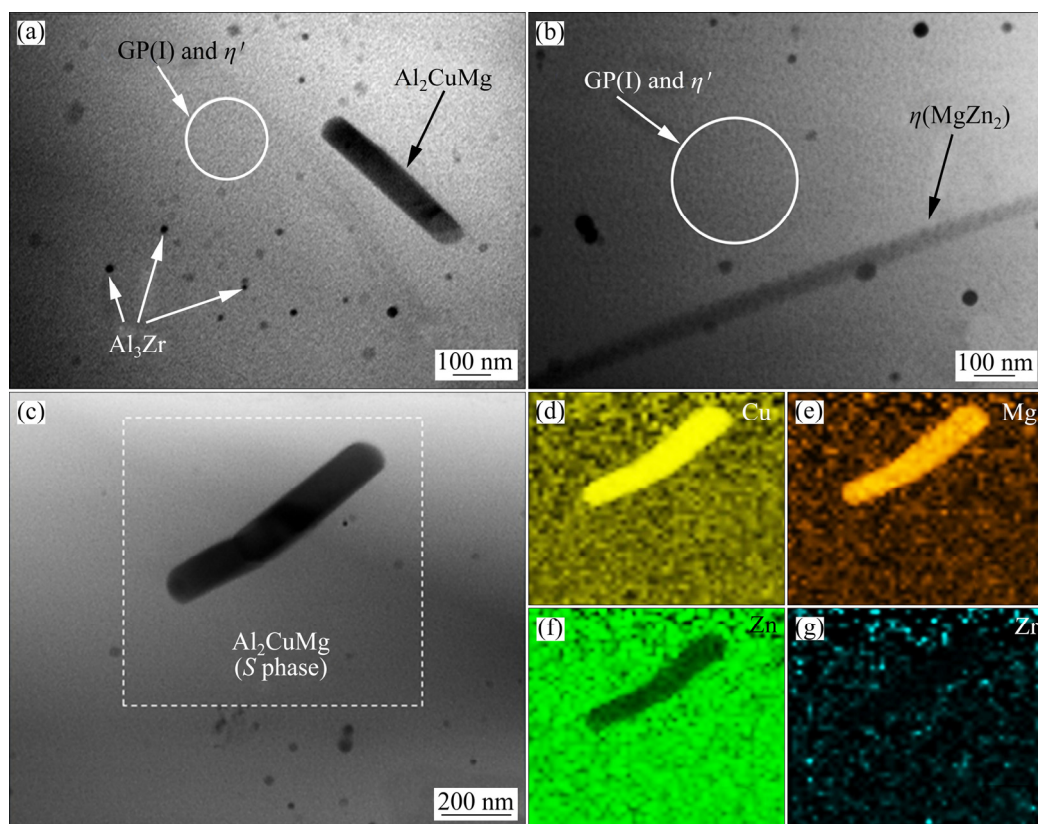


**Fig. 10** TEM bright field micrographs of 7050 alloy wire in aged condition (120 °C, 6 h) showing precipitates dispersed in matrix (a) and at grain boundary (b); STEM bright field (BF) image (c) of *S* phase constituent particle and  $Al_3Zr$  very fine nanoscale precipitates together with respective X-ray elemental maps using EDS ((d) Cu, (e) Mg, (f) Zn and (g) Zr)

and vacancies [32], which also favors homogeneous nucleation of precipitates. The grain boundary precipitates are believed to be the  $\eta$  equilibrium phase, which were favored by heterogeneous nucleation in these high-energy sites. MAZZER et al [8] have also reported  $\eta$  formation at grain boundaries without noticeable PFZ after aging of the extruded AA7050 recycled bar at 121 °C for 16 h.

The elemental X-ray mappings (Figs. 10(d–g)) show the distribution of the elements Cu, Mg, Zn and Zr corresponding to the STEM micrograph (Fig. 10(c)). The distribution of a larger amount of Zn in matrix precipitates can be observed, as well as reasonable amounts of Mg and Cu. Therefore, finely dispersed nanometric precipitates containing Zn, Mg and Cu exist, showing the formation of strengthening precipitates throughout the Al matrix. The high concentration of Cu and Mg can also be seen highlighting the rod-like phase, and indicating it to be related to the  $S$  phase ( $Al_2CuMg$ ) previously indexed in the XRD analysis. Moreover, the X-ray mapping presented in Fig. 10(g) shows several spherical concentrations of Zr, which are associated to the  $Al_3Zr$  dispersoid phase. These cubic, coherent and spherical dispersoids are believed to stabilize the fine-grained microstructure due to the grain boundary pinning effect [7]. As shown previously in the SEM images, the aged wire presented an average grain size around 9  $\mu m$ . This fine-grained structure is attributed to the presence of these fine and evenly placed dispersoids, which pinned grain boundaries during the high-temperature solution treatment, preventing the grains from growing excessively.

### 3.4 Mechanical behavior

Figure 11 shows the aging curve at 120 °C for the 7050 reprocessed alloy previously solution-treated at 470 °C for 0.5 h. A fast increase in hardness values can be seen in the first 2 h of aging, reflecting the rapid growth of zones during artificial aging as these nanometric precipitates are effective barriers to dislocation movement. This strong response to aging is also an indication that solution treatment was effective to provide a supersaturation of alloying elements, which readily clustered into GP zones. The peak-aged condition was attained after aging for 24 h. Thus, aging treating the reprocessed 7050 alloy at 120 °C for 6 h represents

a slightly underaged condition. Although tensile strength may be smaller if compared to a peak-aged condition, there is evidence that underaged conditions yield higher fatigue properties in high-strength aluminum alloys [35]. Vickers hardness of the as-swaged, solution-treated and aged conditions were HV 164, 126 and 174, respectively.

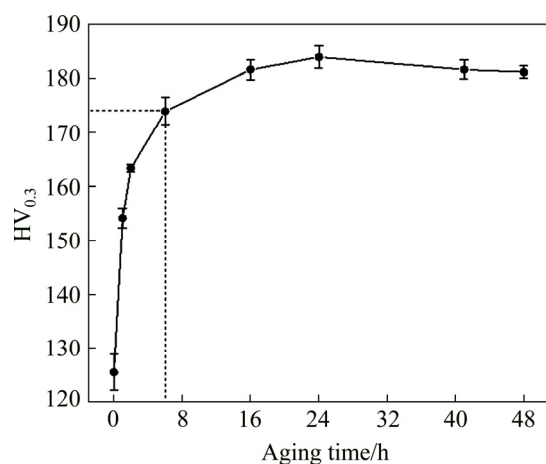


**Fig. 11** Aging curve at 120 °C for 7050 reprocessed alloy previously solution-treated at 470 °C for 0.5 h

Room temperature tensile testing results for the as-swaged and aged (120 °C, 6 h) conditions are presented in Table 2. The aged condition presented higher values of ultimate tensile strength (UTS), elongation and reduction in area, which were, respectively, 9%, 14% and 32% greater compared to those for the as-swaged condition. The higher tensile strength of the aged condition is attributed to the finely precipitated GP(I) zones and primarily  $\eta'$  metastable phase. Both conditions presented high values of elongation and reduction in the area, showing evidence of the excellent ductility of the recycled wires. Despite the severely deformed structure, the as-swaged condition was able to withstand an extensive plastic strain before fracture, which may be attributed to the extremely fine structure resulting from swaging, and also to the refinement of intermetallic phases provided by the thermomechanical processing. Regarding the aged condition, ductility was favored by the fine recrystallized grain structure and the lower work-hardening effect associated to the shearing of nano-sized coherent precipitates [1]. The greater reduction in area attained by the aged specimens may be attributed to the dissolution of the coarser intermetallics (precipitated during thermo-mechanical processing) promoted by the solution

treatment. It is worth pointing out that both wire conditions comply with the original AA 7050 specification for the aircraft manufacturer supplier, AMS 4050J [36].

**Table 2** Tensile testing results for 7050 reprocessed alloy

Material	YS/ MPa	UTS/ MPa	Elongation/ %	Reduction in area/%
7050 as-swaged	476±17	536±24	14±1	25±5
7050 aged	465±6	586±7	16±1	33±3
AMS 4050J	441	510	10	–

Table 3 presents the fatigue testing results obtained from the staircase method for each condition, where  $\sigma_f$  is the estimated average fatigue strength corresponding to a fatigue life of  $10^6$  cycles. In addition, Fig. 12 shows the staircase testing graphically. Both conditions showed good fatigue strength under high cycle fatigue regime. According to the Dixon–Mood statistical approach, the fatigue strength in terms of maximum stress of the as-swaged condition at  $10^6$  cycles was calculated to be  $(165\pm 11)$  MPa. For the aged condition, the calculated fatigue strength was  $(198\pm 7)$  MPa (Svensson–Lorén factor corrected standard deviation) [19]. Therefore, the solution and aging heat treatment of the as-swaged material yielded 20% increase in fatigue strength, and apparently it also helped to minimize fatigue data scatter. The improved fatigue strength is associated to the microstructure optimization for the aged condition, which presents uniform equiaxed grains with a reduced dislocation density due to the full recrystallization taking place. Clean grains can sustain newly-nucleated dislocations, favoring

**Table 3** Staircase testing results

Specimen No.	As-swaged		Aged	
	$\sigma_{\max}$ /MPa	Cycle	$\sigma_{\max}$ /MPa	Cycle
1	170	$5.2\times 10^5$	200	$6.1\times 10^5$
2	160	$1.0\times 10^6$	190	$1.0\times 10^6$
3	170	$1.0\times 10^6$	200	$1.0\times 10^6$
4	180	$5.8\times 10^5$	210	$7.3\times 10^5$
5	170	$4.8\times 10^5$	200	$9.0\times 10^5$
6	160	$9.5\times 10^5$	190	$1.0\times 10^6$
7	150	$1.0\times 10^6$	200	$1.0\times 10^6$
$\sigma_f$	165		198	

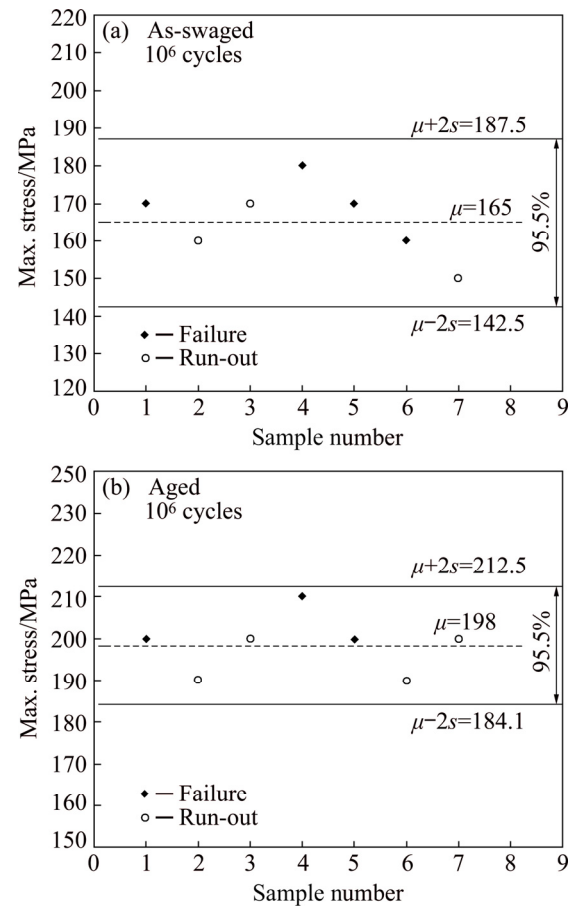


**Fig. 12** Plot of staircase testing results for samples under as-swaged (a) and aged (b) conditions

strain-hardening ability during cyclic loading [37]. These factors minimize cyclic softening and fatigue damage localization, consequently improving fatigue strength [37,38]. Additionally, the inhomogeneous slip associated with the presence of the nanoscale coherent and semi coherent GP(I) zones and  $\eta'$  phase in the aged condition favors slip reversibility of deformation [39,40], yielding lower crack growth rates.

Furthermore, the reduced data dispersion may be ascribed to the dissolution of coarser intermetallics by solution treatment, and the subsequent controlled precipitation of nanoscale strengthening precipitates, which resulted in a more homogeneous microstructure. The lower fatigue strength for the as-swaged condition is related to limited strain-hardening capability due to high dislocation density typical of SPDed materials [37], resulting in cyclic softening, fatigue damage localization, reduced tolerance to preexistent surface flaws and increasing fatigue crack growth rates [15].

In the fatigue experiments reported here, all crack initiation sites were at the surface defects introduced by the swaging process. Therefore, the fatigue strength of the 7050 recycled wire may be improved by an optimization of swaging parameters aiming to provide a better surface finish. Additionally, there was no indication that the constituent particles facilitated the crack nucleation or propagation for the tested conditions, which may be ascribed to the secondary phase refinement promoted by the spray forming technique and the further thermomechanical processing.

## 4 Conclusions

(1) An effective technological route for converting 7050 aluminum alloy scrap into a semi-finished high-strength wire was presented. The mechanical properties attained for the recycled product outperformed the requirements for aerospace application of the original alloy.

(2) The aim was to obtain high tensile strength without adversely affecting ductility and fatigue strength, allowing the 7050 recycled alloy to be considered for structural applications. The microstructural and mechanical requirements for achieving this objective were supported by the results of this work.

(3) Cold rotary swaging the hot-extruded alloy resulted in a severely plastically-deformed and fine-grained microstructure. The grains were elongated and had their diameter reduced to less than 1  $\mu\text{m}$ . Full recrystallization was observed after 30 min of solution heat treating. Equiaxed grains with an average size of 9  $\mu\text{m}$  were obtained.

(4) The results indicated that the aging treatment at 120 °C yields the precipitation of GP(I) zones and a high volume fraction of  $\eta'$  phase. By dissolving coarser intermetallics and promoting the formation of nanoscale strengthening precipitates, the solution and aging treatments favored the formation of a homogeneous structure, imparting higher tensile and fatigue properties.

(5) GP(II) zones and PFZ were not observed after aging the alloy at 120 °C, despite the presence of  $\eta(\text{MgZn}_2)$  equilibrium phase precipitates at grain boundary.

(6)  $\text{Al}_3\text{Zr}$  dispersoids were observed as randomly distributed spherical precipitates ranging from 10 to 40 nm.

## Acknowledgments

This work was supported by CAPES, FINEP (FINEP/CTENERG: 01.09.0485.00), a FAPESP Project (2013/05987-8) and a BPE grant awarded to C.R.M. Afonso (2015/19978-6). The authors are also grateful to Claudemiro BOLFARINI for the material; Leonardo C. CAMPANELLI from CCDM (Center for Characterization and Development of Materials); and IAE (Brazilian Aerospace Institute).

## References

- [1] POLMEAR I J. Light alloys [M]. 4th ed. Oxford: Butterworth-Heinemann, 2006.
- [2] HYODO A, BOLFARINI C, TOSHIMI T. Chemistry and tensile properties of a recycled AA7050 via spray forming and ECAP/E [J]. *Materials Research*, 2012, 15: 739–748.
- [3] DAS S K, KAUFMAN J G. Recycling aluminum aerospace alloys [C]/Light Metals, Annual Meeting & Exhibition. Orlando: TMS, 2007: 1161–1165.
- [4] DIXIT M, MISHRA R S, SANKARAN K K. Structure–property correlations in Al 7050 and Al 7055 high-strength aluminum alloys [J]. *Materials Science & Engineering A*, 2008, 478: 163–172.
- [5] FERRARINI C F, BOLFARINI C, KIMINAMI C S, BOTTA W J F. Microstructure and mechanical properties of spray deposited hypoeutectic Al–Si alloy [J]. *Materials Science & Engineering A*, 2004, 377: 577–580.
- [6] BERETA L A, FERRARINI C F, KIMINAMI C S, BOTTA W J F, BOLFARINI C. Microstructure and mechanical properties of spray deposited and extruded/heat treated hypoeutectic Al–Si alloy [J]. *Materials Science & Engineering A*, 2007, 451: 850–853.
- [7] SHARMA M M. Microstructural and mechanical characterization of various modified 7XXX series spray formed alloys [J]. *Materials Characterization*, 2007, 59: 91–99.
- [8] MAZZER E M, AFONSO C R M, BOLFARINI C, KIMINAMI C S. Microstructure study of Al 7050 alloy reprocessed by spray forming and hot-extrusion and aged at 121 °C [J]. *Intermetallics*, 2013, 43: 182–187.
- [9] GODINHO H A, BELETATI A L R, GIORDANO E J, BOLFARINI C. Microstructure and mechanical properties of a spray formed and extruded AA7050 recycled alloy [J]. *Journal of Alloys and Compounds*, 2014, 586(S): s139–s142.
- [10] MAZZER E M, AFONSO C R M, GALANO M, KIMINAMI C S, BOLFARINI C. Microstructure evolution and mechanical properties of Al–Zn–Mg–Cu alloy reprocessed by spray-forming and heat treated at peak aged condition [J]. *Journal of Alloys and Compounds*, 2013, 579: 169–173.
- [11] GUERRA A P B, ELLENDT N, UHLENWINKEL V, SILVA P S C P, BOLFARINI C. Microstructure of a recycled AA7050 alloy processed by spray forming followed by hot extrusion and rotary swaging [J]. *Materialwissenschaft und Werkstofftechnik*, 2014, 45: 568–573.

- [12] AFONSO C R M, BOLFARINI C, KIMINAMI C S, BASSIM N D, KAUFMAN M J, AMATEAU M F, EDEN T J, GALBRAITH J M. Amorphous phase formation in spray deposited AlYNiCo and AlYNiCoZr alloys [J]. *Scripta Materialia*, 2001, 44: 1625–1628.
- [13] GRANT P S. Spray forming [J]. *Progress in Materials Science*, 1995, 39: 497–545.
- [14] ABDULSTAAR M A, EL-DANAF E A, WALUYO N S, WAGNER L. Severe plastic deformation of commercial purity aluminum by rotary swaging: Microstructure evolution and mechanical properties [J]. *Materials Science & Engineering A*, 2013, 565: 351–358.
- [15] ABDULSTAAR M, MHAEDE M, WOLLMANN M, WAGNER L. Investigating the effects of bulk and surface severe plastic deformation on the fatigue, corrosion behaviour and corrosion fatigue of AA5083 [J]. *Surface & Coatings Technology*, 2014, 254: 244–251.
- [16] PIWEK V, KUHFUSS B, MOUMI E, HORK M. Light weight design of rotary swaged components and optimization of the swaging process [J]. *International Journal of Material Forming*, 2010, 3: 845–848.
- [17] ASTM E112. Standard test methods for determining average grain size [S]. West Conshohocken: ASTM International, 2013.
- [18] ISO 12107. Metallic materials–fatigue testing–statistical planning and analysis of data [S]. Geneva: ISO, 2012.
- [19] POLLAK R, PALAZOTTO A, NICHOLAS T. A simulation-based investigation of the staircase method for fatigue strength testing [J]. *Mechanics of Materials*, 2006, 38: 1170–1181.
- [20] DIXON W J, MOOD A M. A method for obtaining and analyzing sensitivity data [J]. *Journal of the American Statistical Association*, 1948, 43: 109–126.
- [21] MORRISSEY R, NICHOLAS T. Staircase testing of a titanium alloy in the gigacycle regime [J]. *International Journal of Fatigue*, 2006, 28: 1577–1582.
- [22] PAYNE J, WELSH G, CHRIST R J Jr, NARDIELLO J, PAPAZIAN J M. Observations of fatigue crack initiation in 7075-T651 [J]. *International Journal of Fatigue*, 2010, 32: 247–255.
- [23] MONDAL C, MUKHOPADHYAY A K. On the nature of  $T(\text{Al}_2\text{Mg}_3\text{Zn}_3)$  and  $S(\text{Al}_2\text{CuMg})$  phases present in as-cast and annealed 7055 aluminum alloy [J]. *Materials Science & Engineering A*, 2005, 391: 367–376.
- [24] AN X H, LIN Q Y, SHA G, HUANG M X, RINGER S P, ZHU Y T, LIAO X Z. Microstructural evolution and phase transformation in twinning-induced plasticity steel induced by high-pressure torsion [J]. *Acta Materialia*, 2016, 109: 300–313.
- [25] YANG X, LI K, AN X, NI S, WEI W, DU Y, SONG M. Influence of deformation microstructure on the precipitation behaviors of an Al–4Mg–0.3Cu alloy [J]. *Journal of Alloys and Compounds*, 2017, 695: 2238–2245.
- [26] SHA G, YAO L, LIAO X, RINGER S P, DUAN Z C, LANGDON T G. Segregation of solute elements at grain boundaries in an ultrafine grained Al–Zn–Mg–Cu alloy [J]. *Ultramicroscopy*, 2011, 111: 500–505.
- [27] HAN N M, ZHANG X M, LIU S D, HE D G, ZHANG R. Effect of solution treatment on the strength and fracture toughness of aluminum alloy 7050 [J]. *Journal of Alloys and Compounds*, 2011, 509: 4138–4145.
- [28] JIANG X J, NOBLE B, HANSEN V, TAFTO J. Influence of zirconium and copper on the early stages of aging in Al–Zn–Mg alloys [J]. *Metallurgical Transactions A*, 2001, 32: 1063–1073.
- [29] JIANG X J, NOBLE B, HOLME B, WATERLOO G, TAFTO J. Differential scanning calorimetry and electron diffraction investigation on low-temperature aging in Al–Zn–Mg alloys [J]. *Metallurgical Transactions A*, 2000, 31: 339–348.
- [30] MUKHOPADHYAY A K, YANG Q B, SINGH S R. The influence of zirconium on the early stages of aging of a ternary Al–Zn–Mg alloy [J]. *Acta Metallurgica*, 1994, 42: 3083–3091.
- [31] GARCIA-CORDOVILLA C, LOUIS E. A differential scanning calorimetry investigation of the effects of zinc and copper on solid state reactions in Al–Zn–Mg–Cu alloys [J]. *Materials Science & Engineering A*, 1991, 132: 135–141.
- [32] SHA G, CERREZO A. Early-stage precipitation in Al–Zn–Mg–Cu alloy (7050) [J]. *Acta Materialia*, 2004, 52: 4503–4516.
- [33] FAN X G, JIANG D M, MENG Q C, LAI Z H, ZHANG X M. Characterization of precipitation microstructure and properties of 7150 aluminium alloy [J]. *Materials Science & Engineering A*, 2006, 427: 130–135.
- [34] BERG L K, GJONNES J, HANSEN V, LI X Z, KNUTSON-WEDEL M, WATERLOO G, SCHRYVERS D, WALLEMBERG L R. GP-zones in Al–Zn–Mg alloys and their role in artificial aging [J]. *Acta Materialia*, 2001, 49: 3443–3451.
- [35] LUMLEY R N, O'DONNELL R G, POLMEAR I J, GRIFFITHS J R. Enhanced fatigue resistance by underaging an Al–Cu–Mg–Ag alloy [J]. *Materials Forum*, 2005, 29: 256–261.
- [36] AMS4050J. Aluminum alloy, plate 6.2Zn–2.3Cu–2.2Mg–0.12Zr (7050-T7451) solution heat treated, stress relieved, and overaged [S]. Warrendale: SAE International, 2014.
- [37] LIU R, TIAN Y Z, ZHANG Z J, ZHANG P, AN X H, ZHANG Z F. Exploring the fatigue strength improvement of Cu–Al alloys [J]. *Acta Materialia*, 2018, 144: 613–626.
- [38] AN X H, LIN Q Y, WU S D, ZHANG Z F. Improved fatigue strengths of nanocrystalline Cu and Cu–Al alloys [J]. *Materials Research Letters*, 2015, 3: 135–141.
- [39] SHARMA M M, ZIEMIAN C W, EDEN T J. Fatigue behavior of SiC particulate reinforced spray-formed 7XXX series Al-alloys [J]. *Materials & Design*, 2011, 32: 4304–4309.
- [40] de SANCTIS M. Structure and properties of rapidly solidified ultrahigh strength Al–Zn–Mg–Cu alloys produced by spray deposition [J]. *Materials Science & Engineering A*, 1991, 141: 103–121.

# 喷射成形、挤压和旋锻再生处理 7050 铝合金线材的疲劳强度和显微组织

João G. J. de SALVO<sup>1,2</sup>, Conrado R. M. AFONSO<sup>3</sup>

1. Programa de Pós-graduação em Ciência e Engenharia de Materiais (PPG-CEM),  
Universidade Federal de São Carlos (UFSCar), Rod. Washington Luiz, Km 235, 13565-905 São Carlos - SP, Brazil;

2. Divisão de Materiais, Instituto de Aeronáutica e Espaço, CTA,

Praça Marechal Eduardo Gomes, 50, 12228-904 São José dos Campos - SP, Brazil;

3. Departamento de Engenharia de Materiais (DEMa), Universidade Federal de São Carlos (USFCar),  
Rod. Washington Luiz, Km 235, 13565-905 São Carlos - SP, Brazil

**摘要:** 再生高强铝合金由于力学性能差, 在结构材料方面的应用有限。喷射成形重熔后再热挤压是一种有前途的用于 7 系铝合金的再加工方法。对 7050 铝合金切屑进行喷射成形、热挤压、旋锻和热处理, 以恢复其力学性能。制备直径 2.7 mm 的再生铝合金线材, 研究其显微组织、拉伸性能和疲劳强度。采用 XRD、SEM、EBSD、TEM 和 DSC 等手段对二次相和析出相进行表征。对比锻态和热处理(固溶和时效处理)态合金线材的力学性能, 发现两种合金线材的力学性能均优于 AA7050 航空规范。材料在旋锻过程中发生大量的塑性变形, 从而导致急剧的晶粒细化, 可观察到细小的微观和亚微观 Al 晶粒、粗大和细小的金属间化合物析出相。随后的固溶处理导致形成均匀的再结晶和等轴晶(9  $\mu\text{m}$ )显微组织。在 120 °C 时效处理后, 形成纳米级 GP(I) 区和  $\eta'$  析出相, 合金表现出更高的抗拉强度(586 MPa)和疲劳强度(198 MPa)。

**关键词:** Al-Zn-Mg-Cu 合金; 喷射成形; 热机加工; 显微组织; 疲劳

(Edited by Bing YANG)